Microstructure and composition homogeneity, tensile property, and underlying thermal physical mechanism of selective laser melting tool steel parts

Hongyu Chen[a,b], Dongdong Gu[a,b,*], Donghua Dai[a,b], Chenglong Ma[a,b], Mujian Xia[a,b]

[a] College of Materials Science and Technology, Nanjing University of Aeronautics and Astronautics, Yudao Street 29, Nanjing 210016, Jiangsu Province, People's Republic of China
[b] Institute of Additive Manufacturing (3D Printing), Nanjing University of Aeronautics and Astronautics, Yudao Street 29, Nanjing 210016, Jiangsu Province, People's Republic of China

ABSTRACT

This paper systematically investigated the crystallization thermodynamics and dynamic process within melt pool of 5CrNi4Mo steel fabricated by selective laser melting (SLM). The experimental results in conjunction with finite element analysis (FEA) demonstrated that the nucleation rate during SLM process was determined by the combined effects of supercooling degree and transfer capacity of atoms near solid/liquid interface; variant nucleation rate in different region of melt pool caused microstructure heterogeneity. Chemical compositions, including Cr, Ni and C, were observed to be homogeneously distributed due to the rapid solidification of the material. Specimens built along different orientation exhibited discrepant tensile properties due to the different deformation mode during loading. All the as-fabricated SLM-processed tensile specimens showed unfavorable ductility due to heterogeneous microstructures and residual stress concentration. After post-vacuum heat treatment, for horizontally built specimens, the elongation was significantly elevated from 5.6–9.7% and the toughness was enhanced form 63.68 J/m^3 to 134.12 J/m^3. The tensile strength increased marginally from 1576 MPa to 1682 MPa. These promotions were mainly caused by pronounced relief of intrinsic residual stress and recrystallization effect.

1. Introduction

One present trend in manufacture is the reduction in lead times for product development. New processing technologies, especially those in the field of layer by layer additive manufacturing (AM), support this trend [1,2]. Selective laser melting (SLM) is a key AM technology that enables the quick production of complex shaped three-dimensional (3D) parts, which cannot be fabricated by traditional manufacturing methods. Starting with a CAD model of the part, the process proceeds by laser melting sequential powders layers and obtaining the cross-sections of the final product layer by layer, thus achieving direct fabrication of structural or functional parts [3]. Consequently, there is a strong demand across a broad range of sectors, including aerospace, medical, and automotive, for fabricating tailored products with demanded properties by SLM technology [4].

Compared to cast and forged components, there are some specific characteristics in SLM-processed parts, including grain refinement, extended solid solubility, chemical homogeneity and reduction in quantity and size of phase segregation, which contribute to excellent mechanical properties [5]. However, because of the vigorous Marangoni convection induced by high thermal capillary forces, SLM suffers from the instability of the molten pool and thus causing microstructures uncontrollability. Moreover, variant thermodynamics behaviors (e.g. solidification rate, cooling rate and thermal gradient, etc.) at different region of melt pool give rise to microstructural heterogeneity and accordingly have negative effects on the plasticity and toughness of SLM-processed parts. The basic principle of the SLM process in terms of non-equilibrium crystallization and phase transformation process, affected by rapid melting and quenching as well as complicated thermal history within the melt pool, is not yet well understood and requires further investigations.

5CrNi4Mo steel type is a medium-carbon, cold work steel used to make tools for cutting, coining and injection molding. Excellent elastic strength, hardness and wear resistance are all essential properties

---

* Corresponding author at: College of Materials Science and Technology, Nanjing University of Aeronautics and Astronautics, Yudao Street 29, Nanjing 210016, Jiangsu Province, People's Republic of China.
E-mail address: dongdonggu@nuaa.edu.cn (D. Gu).

Table 1
Chemical compositions of as-used 5CrNi4Mo steel powder.

Element	Fe	C	Cr	Ni	Mo	Si	Mn	P	S
Content (wt %)	Balance	0.45	1.35	4.0	0.25	0.25	0.40	≤0.025	≤0.005

when choosing a tool steel. It is well known that microstructures in steel determine its properties. Therefore, before a tool is put into use, it requires tedious heat treatment procedures, like quenching and tempering, to meet the service demand. Interestingly, during SLM process, the considerably large cooling rate in melt pool can directly induce martensite transformation without any heat treatment. As such, SLM is a good method to avoid these follow-up processes but still obtain demanded properties, which can not only guarantee quenching quality, but also lower costs and shorten cycle times. Colaco et al. [6] took advantages of laser surface melting (LSM) technology to directly obtain martensite with high proportions of above 80% by optimizing composition and processing parameters. Nevertheless, the repeated rapid heating and cooling during laser processing generally resulted in large residual thermal stress in the workpieces, which would have a considerable influence on the mechanical properties of laser-processed parts and significantly limit their industrial applications. AlMangour et al. [7] and Badrossamay et al. [8] prepared tool steels using SLM and indicated that the tool steels were challenging to process because the parts with high-strength and low toughness were greatly susceptible to cracking. Holzweissig et al. [9] reported on SLM processing of ferritic/ martensitic steels without post-heat treatments and demonstrated the unpredictability of microstructures of tool steels due to repetitive heat flux during melting of overlying powder layers.

Based on the previous works conducted in different types of steels concerning different aspects, such as densification, microstructure and mechanical properties investigations [4–9], it can be summarized that there are still numerous objects requiring to be illuminated and understood, such as the crystallization process located in different regions of melt pool and the controllability of solidification microstructure of SLM-processed tool steel parts. Therefore, the melt pool dynamics and solidification process during SLM were deeply investigated in this paper, so as to reveal the nucleation mechanism and forming principle of microstructure heterogeneity of SLM-processed parts. The elements segregation behavior was also studied and compared to other researches, because the extent of elements segregation can severely affect the load-bearing capacity of structural components [10]. In addition, based on the available published literatures, there are little previous studies focusing on the investigations of ultimate strength and ductility of SLM-processed tool steel part. Authors believed that the tensile property characterization is of great significance because the inherited major stresses in SLM-processed parts will negatively influence the strength and strain if the stress is not relieved. As such, a post-vacuum heat treatment was also conducted in this paper and the tensile properties of as-fabricated and heat-treated

were compared.

2. Experimental procedures

2.1. Powder materials and SLM process

Spherical gas-atomized 5CrNi4Mo steel powder was used in this study with a mean particle size of 21.6 µm and the chemical compositions are listed in Table 1. The SLM system was independently developed and consisted mainly of a YLR-500 ytterbium fiber laser with a power of ~500 W and a spot size of 70 µm (IPG Laser GmbH, Germany), an automatic powder layering device, an inert argon gas protection system, and a computer system for process control. A stainless steel substrate plate was horizontally fixed on the building platform during the whole SLM process with a dimension of 150 mm×150 mm×30 mm. In order to obtain samples with satisfactory densification level, the laser power (P) was set at 77.5 W. Layer thickness (h) and hatching spacing (s) were set at 30 µm and 50 µm respectively, based on a series of preliminary experiments. Meanwhile, various scan speeds (v) were set by the SLM control program, in order to change the processing conditions during one batch of experiments. The applied laser volume energy density η, which was defined by [11]:

$$\eta = \frac{P}{vsh} \tag{1}$$

were used to assess the laser energy input to the powder layer being processed.

2.2. Microstructural characterisation and mechanical testing

The Archimedes principle was used to measure the density of the specimens. Phase identification was performed by X-ray diffraction (XRD) using a D8 Advance X-ray diffractometer (Bruker AXS GmbH, Germany) with Co Ka radiation at 40 kV and 40 mA, using a continuous scan mode. A scan at 2°/min was conducted over a wide range of $2\theta=30–85°$ to give a general overview of the diffraction peaks. Samples for metallographic examinations were cut, ground and polished according to standard procedures and etched with a solution consisting of HNO_3 (4 ml) and CH_3CH_2OH (96 ml) for 20 s. Microstructures were characterized using a PMG3 optical microscopy (Olympus Corporation, Japan) and a S-4800 field emission scanning electron microscope (FE-SEM) (Hitachi, Japan) at 3 kV.

Tensile samples were fabricated both vertically and horizontally for mechanical testing according to the standard of GB/T228-2010 (Fig. 1). Some of the SLM-processed samples were also heat treated to study the influence of post heat treatment on mechanical properties. A post-vacuum heat treatment was used which included heating of samples from room temperature up to 640 °C with a heating rate of 10 °C/min and dwelling at 640 °C for 3 h and then cooled within the furnace to the room temperature. The tensile test was conducted at room temperature on a CMT5205 testing machine (MTS Industrial Systems, China) at a cross head velocity of 2 mm/min. The toughness of material which could show the ability to absorb mechanical energy of
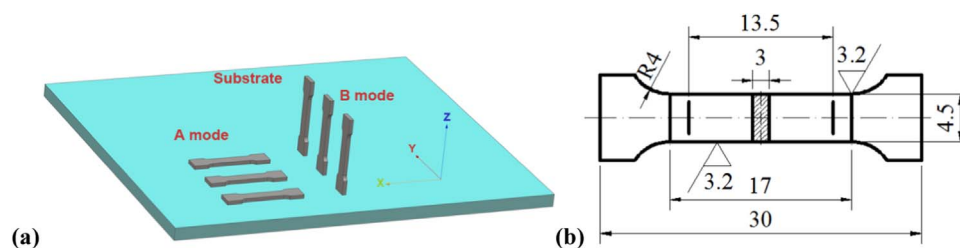

Fig. 1. (a) 3D view of the tensile test specimens: A horizontal build-up; B vertical build-up. Geometry of SLM processed sample for tensile testing (b).

Table 2
The as-used material properties and SLM processing parameters.

Parameters	value
Laser absorptivity of the iron-based powder	0.47[8]
Ambient temperature, T_0	300 K
Surface tension, γ	[1909−0.52 (T - 1803)] × 10^{-3} N/m T& $2gt;1803$ K[16]
Marangoni coefficient, $\partial\gamma/\partial T$	-0.52×10^{-3} N/(m K)
Powder layer thickness, h	30 µm
Hatching space, s	50 µm
Radius of the laser beam, ω	35 µm
Laser power, P	77.5 W
Scan speed, v	200, 300, 400 mm/s

material in its unit volume up to failure was obtained by calculating the area underneath the stress-strain curve [12,13]. The tensile fracture surfaces were also observed by FE-SEM.

3. Finite element simulation

Finite element analysis (FEA) using the computational fluid dynamics software FLUENT 6.3.26 was conducted to predict the melt pool geometry, quasi-stationary temperature field for single tracks and the velocity vector plots in the melt pool with the action of Marangoni effect. Meanwhile, the temperature variation of different districts of melt pool during the solidification process was detected in order to obtain a thorough understanding of the temperature evolution behavior during the SLM process. The as-used material properties and SLM processing parameters are shown in Table 2.

The Gaussian laser source, which moved at a constant rate along the X-axis, was performed on the powder layer, assumed by the absorption phenomenon in the skin layer. The model used in this investigation has been described in detail by our previous works [14,15].

4. Results and discussion

4.1. SLM-processed 5CrNi4Mo steel parts

Fig. 2a shows the influence of η on the relative density of the SLM samples. It was found that the highest relative density was obtained when the η was settled at 215.28 J/mm³ (v=300 mm/s). Therefore, the SLM parts prepared at 215.28 J/mm³ were chosen to study the homogeneity of microstructure and mechanical property of SLM-processed tool steel. High accuracy blades were successfully fabricated

from 5CrNi4Mo steel powders for applications in aerospace and automobile industries, showing a good surface finish without macroscopic balling phenomenon and dimensional distortion (Fig. 2b).

4.2. Verification of accuracy of simulated results by experimental investigations

The temperature distribution plot of the top surface of melt pool, as the η is settled at 215.28 J/mm³, is shown in Fig. 3a. It could be found that the melt pool and heat-affected zone (HAZ) had an elongated shape in the scanning direction. The ellipse shape instead of circular shape was believed to be caused by the movement of heat source, which was also discussed by Wang et al. [17]. In order to verify the accuracy of simulated results, the cross-sections of melt pools of simulation predicted and experimentally obtained under different η are given in Fig. 3b–d. The results showed that the melt pool shapes obtained by simulation calculation and experiments were observed similar and there were few distinctions in width and depth. The calculated maximum temperature T_m of the melt pool varied from 2765 K at 161.46 J/mm³ to 2847 K at 322.92 J/mm³, which was close to the T_m of 316 L stainless steel about 2740 K [18]. Fig. 4 demonstrates a high degree of consistency of the simulated and experimentally measured melt pool dimensions under various η, which further validates the accuracy of the simulation models. Therefore, the FEA provides a good method for predicting the densification of the SLM parts before experiment. According to Su et al. [19]'s research, in order to obtain a continuous substance, the tracks must fill up nominal volume being fabricated. Assume that each single melting track shape is the same and ignore the thermal expansion of HAZ, pore capture and balling effect, an approximate expression can be obtained as follows:

$$\frac{L_w}{2}f_h^{1/2} \geq \frac{s}{2}(0 < f_h^{1/2} < 0.5) \tag{2}$$

$$\frac{L_w}{2}f_h^{1/2} + \frac{L_w}{2}(2f_h^{1/2} - 1)^{1/2} \geq \frac{s}{2}(0.5 \leq f_h^{1/2} < 1) \tag{3}$$

where L_w is the width of melting track, the inter-layer overlapping rate f_h =(L_d-h)/h, L_d is the depth of melting track. Eq. (2) and Eq. (3) indicate that the densification of SLM parts is mainly influenced by the inter-layer overlapping rate f_h and the width of melt pool L_w. As the η is settled at 215.28 J/mm³, the $f_h^{1/2}$ and L_w are calculated about 0.516 and 82 µm respectively (Fig. 4). Substitute the $f_h^{1/2}$ and L_w into the Eq. (3) and find that Eq. (3) holds in this situation, which indicates that the SLM parts with high densification level can be obtained under this processing parameter. As the η decreases to 161.46 J/mm³, the $f_h^{1/2}$ and L_w are calculated about 0.258 and 75 µm respectively (Fig. 4). Substitute the $f_h^{1/2}$ and L_w into the Eq. (2) and find that Eq. (2) does not hold in this situation, which means the lower densification level
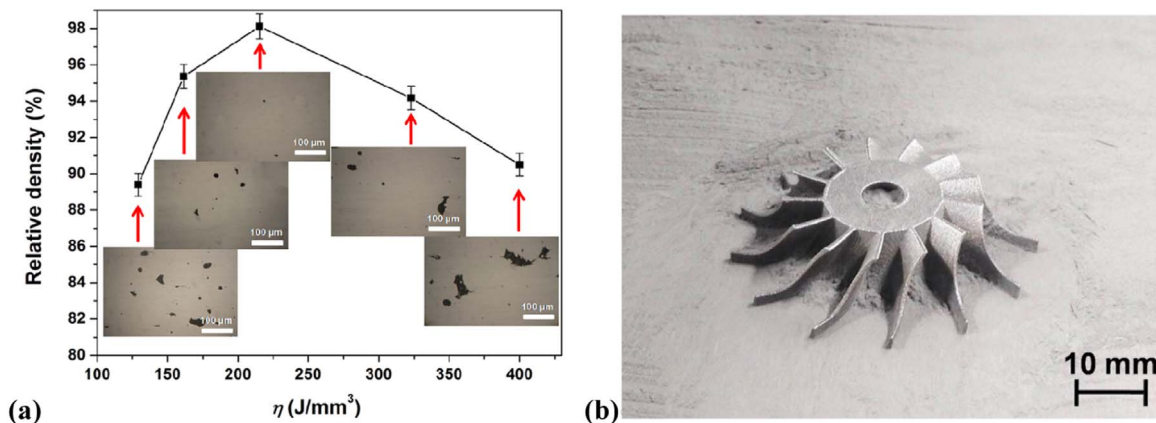

(a)

(b)

Fig. 2. (a) Variation of densification level of SLM-processed parts with different η; (b) High accuracy blades successfully fabricated from 5CrNi4Mo steel powders (η=215.28 J/mm³).

(a)

Fig. 4. The calculated and experimentally measured melt pool dimensions under different η.
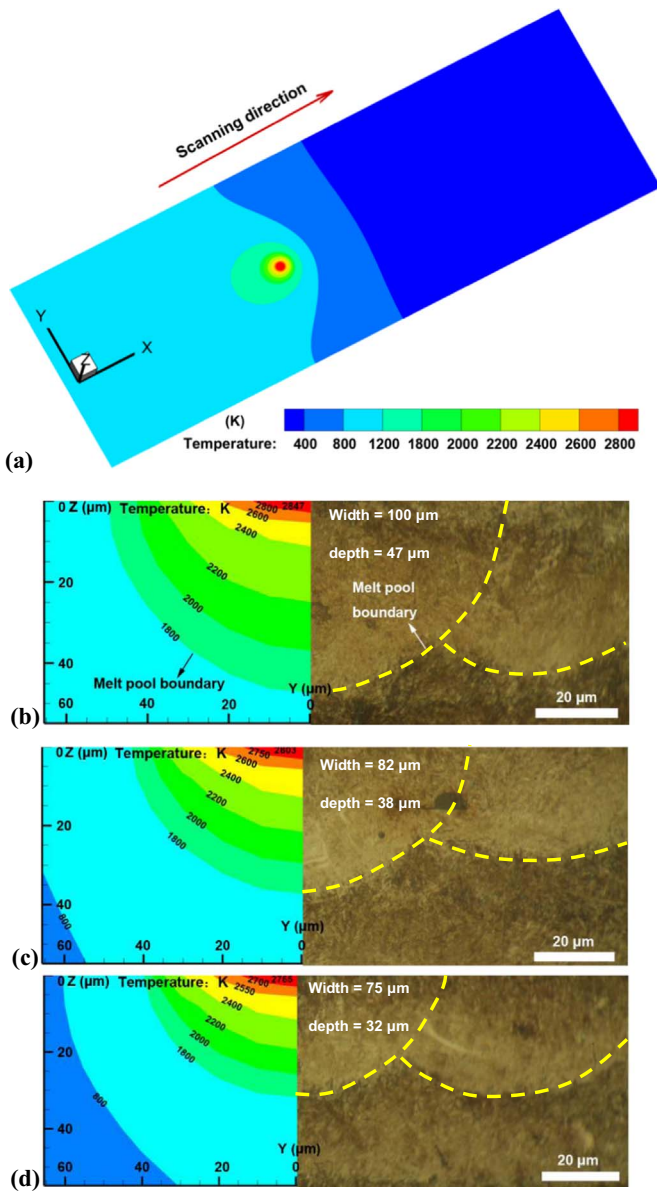

(b)

(c)

(d)

Fig. 3. Temperature contour plots in top view (a) and comparisons of simulated (left) and experimental (right) melt pool profiles on cross-section at different η: (b) 322.92 J/mm³; (c) 215.28 J/mm³; (d) 161.46 J/mm³ (hatching space 50 μm).

and more residual pores, as shown in Fig. 2a. As such, the forming quality of the SLM-processed parts can be accurately predicted by FEA. An optimized processing window can be made before experiment in order to alleviate the occurrence of defective items and avoid unnecessary expense.

4.3. Microstructure homogeneity

Since each layer is successfully completed by a favoring lapping of adjacent melting tracks, the microstructure homogeneity of SLM-processed parts can be determined by characterizing one single melting track. Fig. 5a shows the cross-section of a single melt pool with three zones: bottom zone, center zone and top zone, divided by the white fine dash line and the yellow heavy dash line. The FE-SEM images at higher magnification, as shown in Fig. 5b–d, give characteristic morphologies of the martensitic microstructure located in these different zones. It was found that, in the bottom zone near the melt pool boundary, ultrafine martensite lath bundles were obtained with a mean lath width
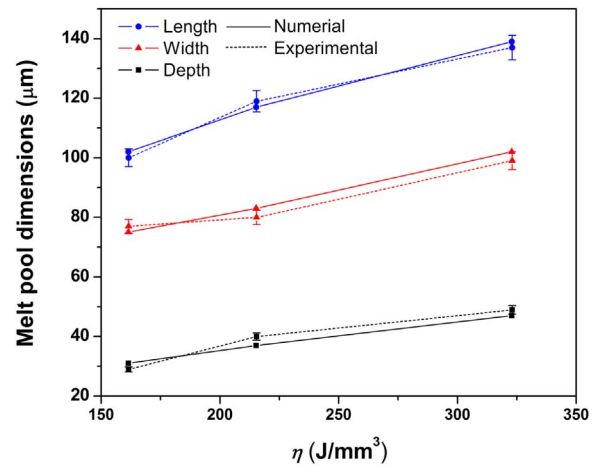
smaller than 0.4 μm (Fig. 5b). In contrast, the microstructures in the center of the melt pool were observed to be coarser (Fig. 5c) with an average lath width of about 0.58 μm. Interestingly, in the top zone, martensite was observed to become appreciably coarsed with a mean lath width larger than 1 μm (Fig. 5d). Meanwhile, it seemed to have lost the lath-shaped characteristics to some extent. Therefore, the tool steel parts fabricated by SLM were characterized by a heterogeneous microstructure.

Compared to the traditional manufacturing methods, SLM has significant superiority on account of its rapid melting and solidification nature. It is well established that the SLM-processed parts have finer microstructure compared with the cast and forged parts. This is due to the considerably high cooling rates (10^3–10^8 K/s) of melt pool during the SLM process [20]. Therefore, temperature distribution profiles and cooling rates versus time located in point A, point B and point C (marked in Fig. 5a) are determined in Fig. 6 by FEA method, so as to compare the solidification features of different regions of melt pool. From the curves of cooling rates, it could be found that the value of cooling rates varied from negative to positive when the laser beam approached and left the detected point, corresponding to the melting process and the solidification process of melt pool; The calculated maximum temperature of point A, point B and point C was 2581 K, 2267 K and 2110 K respectively; The calculated maximum cooling rate of point A, point B and point C was 1.19×10^7 K/s, 1.49×10^7 K/s and 1.93×10^7 K/s respectively. As for the phenomenon of grain refinement of SLM-processed parts, numerous investigations indicate that the high cooling rates bring large thermal undercooling and kinetic undercooling to the melt pool. The large undercooling degree within the pool would cause a high nucleation rate and hence refine the microstructures significantly [21–23]. However, according to classical nucleation theory, although a large undercooling ΔT is conducive to nucleation, the rapid decreased temperature of melt pool can considerably circumscribe the activity of solute atoms. This would be to the disadvantage of nucleation. As such, the transfer capacity of atoms from the liquid to the nuclei should be considered. The thermodynamics nucleation rate N_1 mainly influenced by the variation of free energy of.

system can be calculated by:

$$N_1 = K_1 \exp(-\frac{\Delta G^*}{T \Delta T^2})$$

(4)

where K_1 is a constant, ΔG^* is the critical nucleation Gibbs free energy, T is the operative temperature. Eq. (4) indicates that an increase of ΔT can dramatically elevate N_1; even though the T is also decreased, its
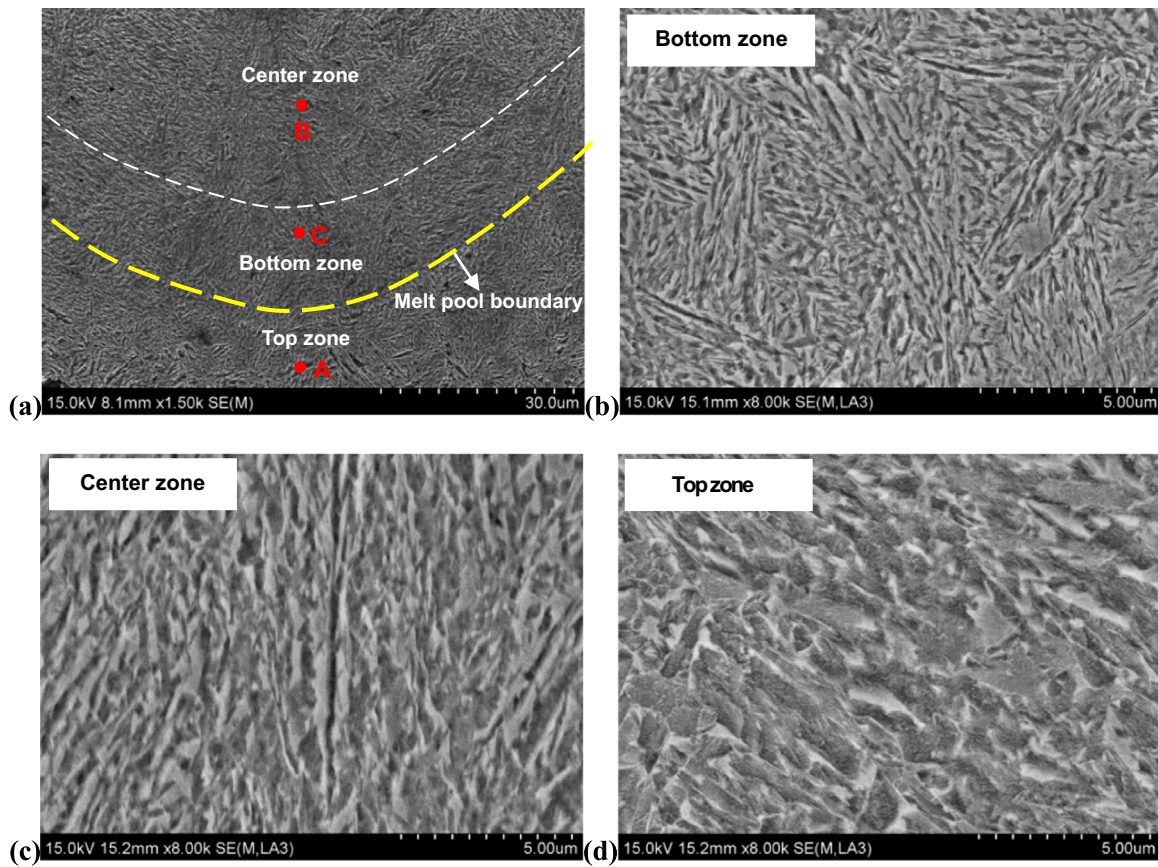
Fig. 5. FE-SEM showing characteristic melt pool on cross-sections of SLM-processed parts (a) and magnified martensitic structure located in different zones: (b) Bottom zone; (c) Center zone; (d) Top zone (η=215.28 J/mm^3). (For interpretation of the references to color in this figure, the reader is referred to the web version of this article.)

influence on N_1 can be negligible. Then, the formation of nuclei will require the transfer of atoms from the liquid to the nuclei. The kinetics nucleation rate N_2 depending on the transfer capacity of solute atoms can be determined by:

$$N_2 = K_2 \exp(-\frac{\Delta G_0}{k_B T}) \tag{5}$$

where ΔG_0 is the activation energy for transferring through the solid/ liquid interface, k_B is the Boltzmann constant and K_2 is a constant when the solid/liquid interface is stable. Nevertheless, the solidification process during SLM is a non-equilibrium process. It is well known that the Marangoni convection within the melt pool has a significant effect on heat and mass transfer, which signally influences the crystal nucleation and growth [17]. The Marangoni flow on the top surface longitudinal-section and cross-section of melt pool is shown in Fig. 7a– c, which exhibits a radially outward flow pattern. Due to the significant temperature gradient within the melt pool, the maximum velocity vector near the melt pool boundary can reach to 0.1 m/s. Consequently, the intense melt flow facilitates the occurrence that the solute atoms are more likely to be transferred to the cores and captured by the tips of dendrites (Fig. 7d). This would significantly accelerate dendrites development. In this situation, the K_2 in Eq. (5) should not be regarded as a constant and Eq. (5) can be expressed as:

$$N_2 = K_2 K_l \exp(-\frac{\Delta G_0}{k_B T}) \tag{6}$$

where K_l is the flux factor depending on the amount of atoms transferred from liquid to solid/liquid interface in unit time. K_l is believed to be in positive correlation with the flow velocity of melt. Based on above thermodynamics and kinetics analyses, the ultimate

nucleation rate N can be expressed as:

$$N = K \exp(-\frac{\Delta G_0}{k_B T}) \times \exp(-\frac{\Delta G^*}{T \Delta T^2}) \times K_l \tag{7}$$

where K is a constant. Eq. (7) indicates that, as the crystallization temperature is fixed, the nucleation rate N is mainly affected by ΔT and K_l. ΔT is controlled by cooling rates as already demonstrated above, while K_l depends on the transfer velocity of solute atoms. In order to determine the transfer velocity of solute atoms in different zones, the maximum liquid flow velocity-magnitude and velocity gradient near the melt pool boundary during the lifetime of melt pool is calculated and shown in Fig. 8. The results illuminate that, at early stage (0– 0.2 ms) corresponding to the solidification process of bottom zone, the flow velocity is relatively high. The attendant velocity gradient is kept low, which means that the melt pool sustains high temperature gradient during this stage. At middle stage (0.2–0.4 ms) corresponding to the solidification process of center zone, the flow velocity gradually decreases and the velocity gradient increases continually to a max- imum, indicating that the temperature gradient of melt pool begins to get smaller and decreases the most quickly at 0.4 ms. At end stage (0.4–0.5 ms) corresponding to the solidification process of top zone, the flow velocity is relatively low and velocity gradient rapidly reduces. This demonstrates that, at the end of the lifetime of melt pool, the temperature distribution between melt pool and solidified part become relatively small by adequate conduction of heat through the substrate. As such, the melt flow is not as significant as above two stages. In conclusion, at the bottom zone of melt pool, the high ΔT could lead to a high thermodynamics nucleation rate and the relatively large K_l guarantees the high activity of solute atoms, hence significantly facilitating the refinement of microstructures. In contrast, the lower
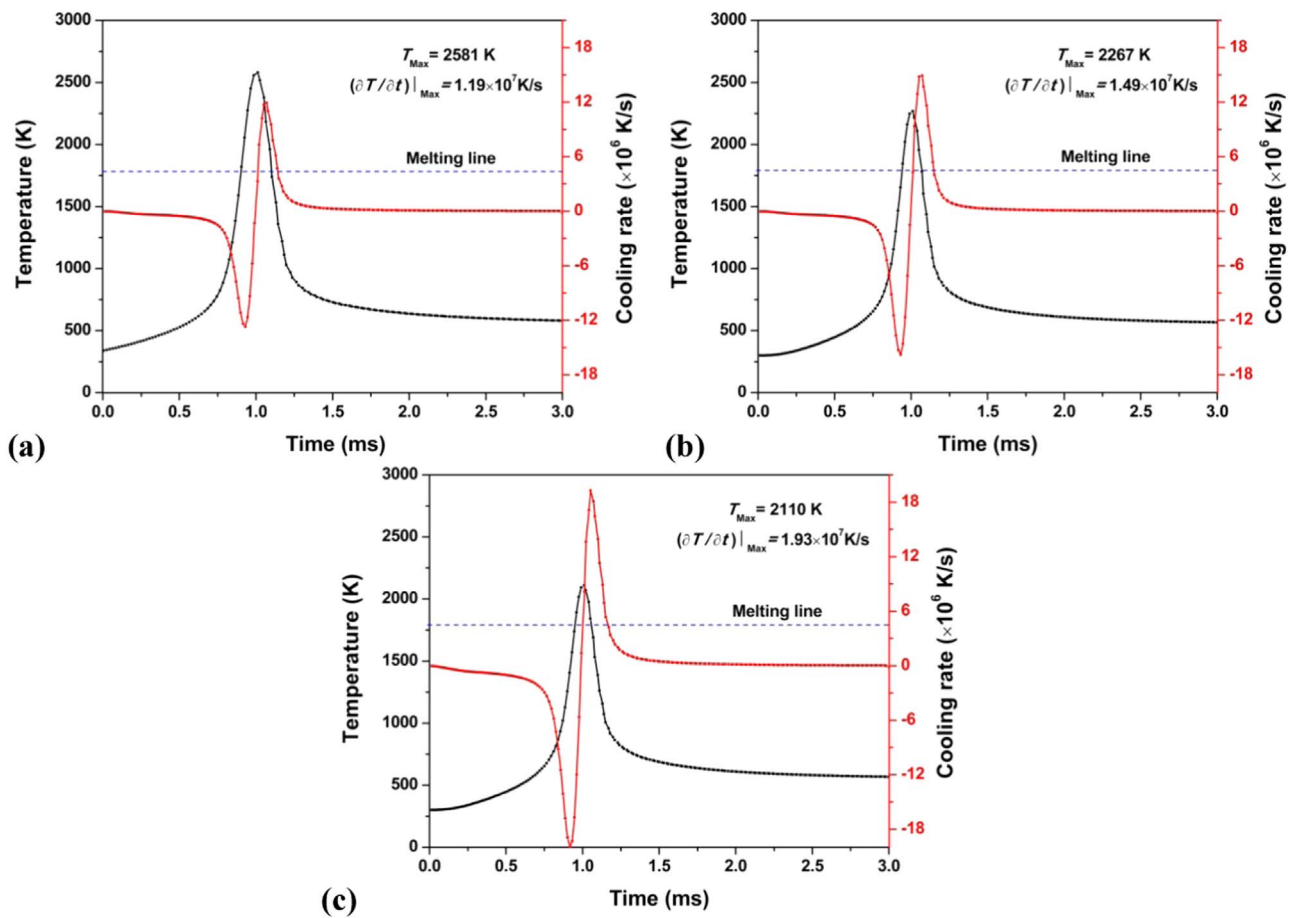
Fig. 6. Temperature distribution profiles and cooling rates versus time at different locations of melt pool: (a) point A; (b) point B; (c) point C.

ΔT and K_1 in the center/top zone imply weaker driving force of crystallization and diffusion ability of solute atoms. This accordingly results in a coarsed microstructure. It is worth noting that, since the SLM is a layer by layer AM process, each layer experiences similar thermal circumstances. This would result in a variational microstructure following a repetitive/alternating phase of martensite and a mixture of martensite/austenite, as reported by Liu et al. [24]. Especially for the top zone of melt pool, the thermal effects from the next processed layer are significant. The effect of tempering tends to occur easily during repetitive heat conduction, hence leading to the further coarsed tempered martensitic structure as shown in Fig. 5d.

4.4. Chemical composition distribution

Due to the high cooling rate and attendant large undercooling during the SLM process, the solidification of melt pool is believed to occur in a partitionless manner, which leads to uniformity of chemical composition [25]. Sander et al. [5] found that the SLM sample revealed a homogeneous distribution of the carbide forming elements Mo, V and Cr. Meanwhile, the much refined carbide network was also identified and the carbides tended to be located at the martensite boundaries. Generally, the carbides forming at the grain boundary bring about high brittleness and poor toughness, accordingly reducing the mechanical properties of steel [26]. Fig. 9 shows the magnified SEM images of the martensite structures in the top zone of melt pool and related EDX mappings showing the element distribution of Cr, Ni and C. In contrast, the carbide network was not found forming in the martensite boundaries in this study and good dispersion of the alloying elements

was obtained (Fig. 9b–d), suggesting the enhanced mechanical properties required for load bearing applications. This distinctive elemental distribution is believed to be caused by rapid solidification of the material that does not allow enough time for diffusion of the alloying elements. Therefore, the carbide formers tend to remain in solid solutions with iron rather than forming carbides. As a result, only martensite and retained austenite were obtained in the solidification microstructures of SLM-processed parts, as shown by the XRD spectra (Fig. 9e).

4.5. Tensile properties

Figs. 10 and 11 show the tensile testing results for the as-built and post-vacuum heat-treated tensile samples fabricated along different orientations. Since the lath-shaped martensite generally has high hardness, good plasticity and toughness, the tensile strength and ductility of the SLM-processed tensile samples are anticipated to be favorable. Nevertheless, it could be seen that both the horizontally and vertically built SLM specimens possessed a very low elongation (5.6% and 4.0%) and a low toughness (63.68 J/m^3 and 27.80 J/m^3), although exhibiting an excellent tensile strength (1576 MPa and 1240 MPa). The cause of the low toughness of SLM-processed tensile parts can be ascribed to three main aspects. First, the heterogeneous microstructures would have great effect on the toughness of SLM-processed parts. Since the effect of grain size on the mechanical properties can be rationalized by Hall-Petch (HP) relationship, the various grain sizes in different zones of melt pool lead to the different extent of the size-induced strengthening effect [27]. Generally, the finer the initial grains,
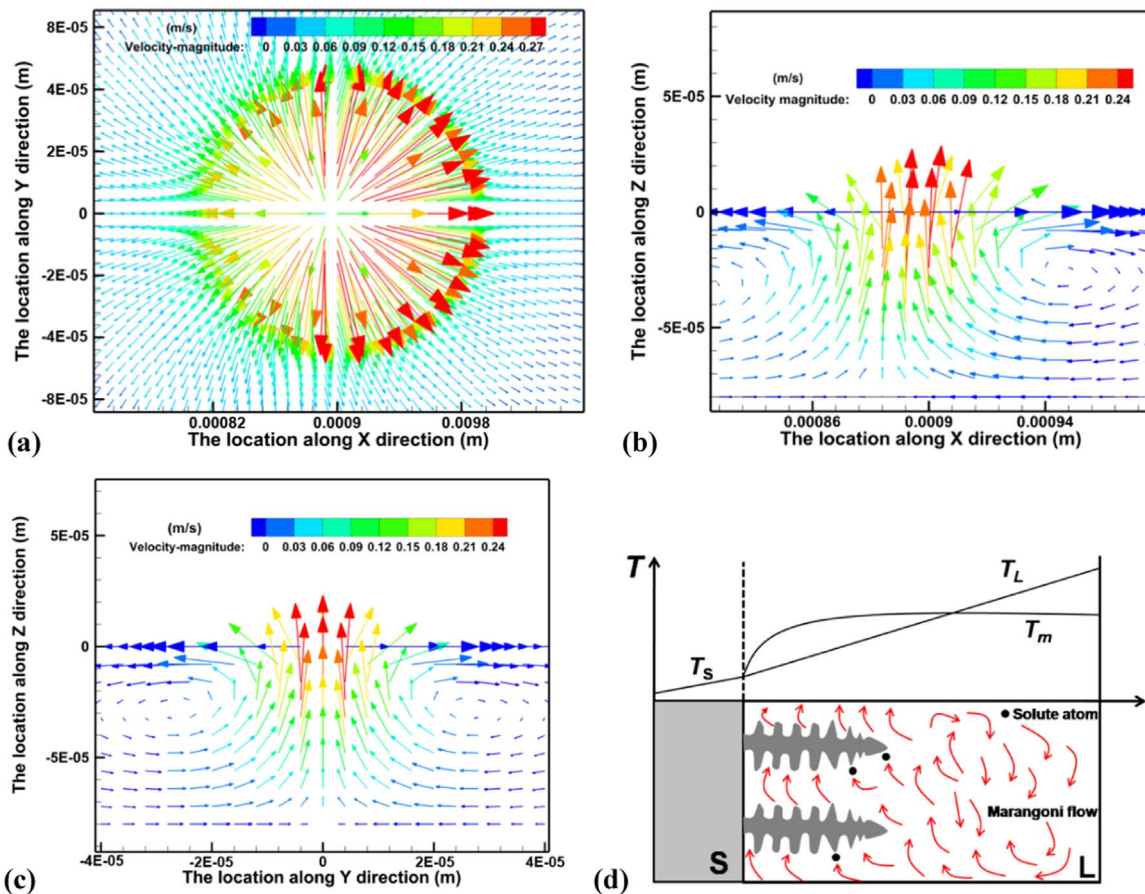
Fig. 7. Velocity vector plots in the melt pool with the action of Marangoni effect in different views: (a) top view; (b) longitudinal view (c) cross-sectional view (η=215.28 J/mm³). The schematic diagram that the Marangoni effect influences the nucleation process during SLM (d).

the more significant the pile-up effect of dislocations at grain boundaries and the larger the resistance of the dislocations to slip transfer. Consequently, when subjected to external forces, the zones of melt pool with finest grains are harder to deform compared with the other zones. This deformation inhomogeneity would cause large stress concentration, hence accelerating the crack source expanding. Secondly, the tensile residual stress and the micro or macro cracks often appear in the overlapping region between two adjacent melting tracks as
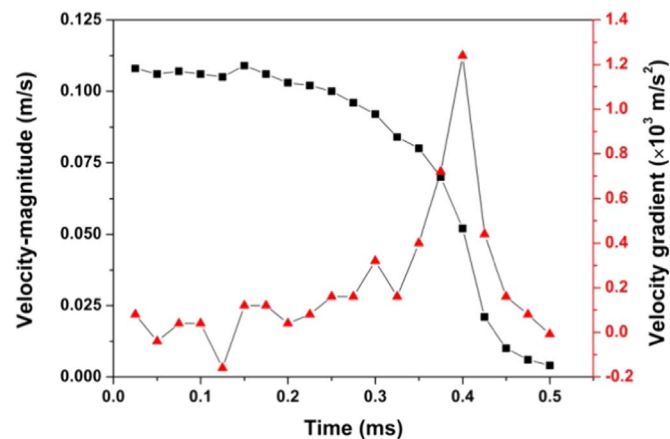
Fig. 8. Maximum liquid flow velocity-magnitude and velocity gradient versus time near the melt pool boundary during the lifetime of melt pool (η=215.28 J/mm³).

demonstrated by previous study [28]. The crack propagation or fracture would easily occur either at the weak material region or at the high stress concentrated area during tensile tests [29], hence giving rise to initial failure. Thirdly, the occurrence of martensitic transformation is generally accompanied by microscopic volume expansion, which in turn creates stresses at grain boundaries and causes pronounced residual stresses among crystalline grains. The stress arising from phase transformation easily concentrates on the grain boundary and brings heavier brittleness to the SLM samples. It was clear that the horizontally as-built samples exhibited not only superior tensile strengths but also better elongations as compared with the vertically as-built samples. In order to further study the fracture mechanism, fracture morphologies of the as-built tensile samples under different built direction are shown in Fig. 12. The fracture surfaces of the vertically as-built samples exhibited obvious "cleavage river pattern" (marked by yellow arrow in Fig. 12b), showing a typical brittle fracture. This was in accordance with the very low toughness as shown in Fig. 10a. In contrast, there were two main morphologies on the fracture surfaces of the horizontally as-built samples: equiaxed dimples and cleavage planes. It was indicative of a ductile as well as a brittle failure. The origin for the difference in tensile properties of iron-based parts among different built direction was elucidated by Qiu et al. [30]. Their work indicated that the variation in the fracture feature among the samples built along different directions was caused by the difference in loading mode, i.e., the loading direction relative to the orientation of the planar residual pores and cracks. Because of "balling effect" and large residual stress, the pores and cracks have a high tendency to form along the interlayer. As the direction of tensile force is normal to the
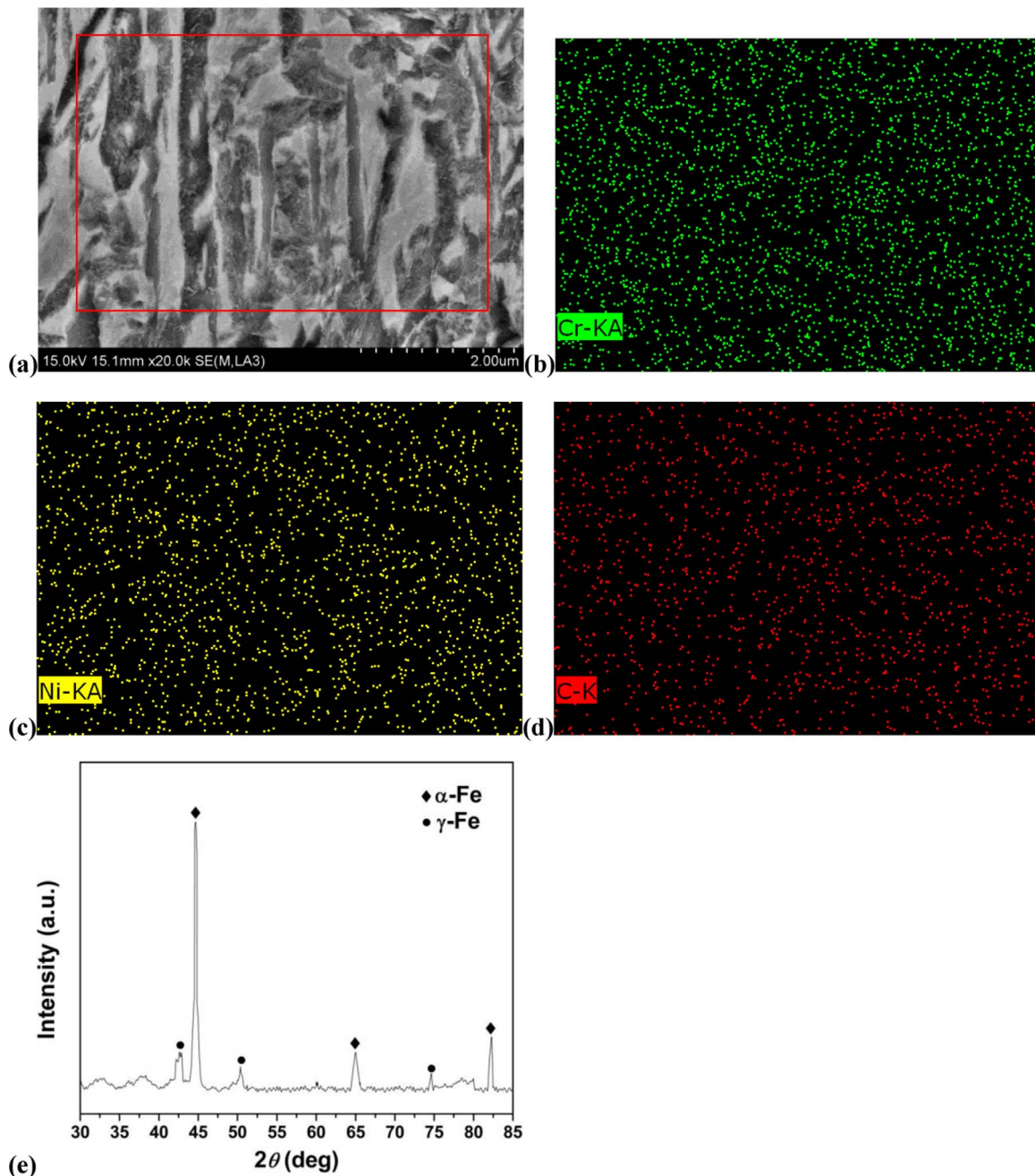
Fig. 9. Magnified SEM images of the martensite structures (a) and related EDX mappings showing the element distribution of Cr (b), Ni (c) and C (d). (e) XRD spectra of SLM-processed parts at, over a range of 2θ (30–85°) (η=215.28 J/mm^3).

orientation of the pores and cracks, the interlayer with defects moves directly apart, corresponding to an "opening or tensile mode". As the direction of tensile force is almost parallel to the planar pores or cracks, the loading mode turns into a "sliding or in-plane shear mode". The opening/tensile mode appreciably results in earlier failure compared with the sliding/in-plane shear mode. Hence, the vertically as-built samples possess inferior tensile strengths compared with horizontally built ones.

After heat treatment at 640 °C for 3 h, there was a considerable improvement in ductility, while the variation in strength was small. For the horizontally built specimens, a significant increase in elongation from 5.6–9.7% could be observed; the toughness was enhanced to 134.12 J/m^3; the tensile strength was elevated marginally from 1576 to 1682 MPa. The fracture morphologies of the heat-treated tensile

samples under different built directions are given in Fig. 13. The equiaxed dimples with an average size about 1 μm were observed across the whole fracture surface, showing a highly ductile fracture. Generally, the microstructure transformation from martensite to tempered sorbite can lead to the improvement in ductility, but always result in a decrease in hardness and strength. Interestingly, all of the mechanical performance indexes (e.g. tensile strength, elongation and toughness) have been improved in this experiment. A post-vacuum heat treatment of SLM samples can be beneficial in three ways. First, the heat treatment is inclined to improve the microstructural homogeneity. This would lead to a uniform distribution of refined ferrite and granular cementite, hence enhancing the integrated mechanical properties. Secondly, since the heat treatment has a great function of reducing the internal stress of workpiece, the pronounced relief of
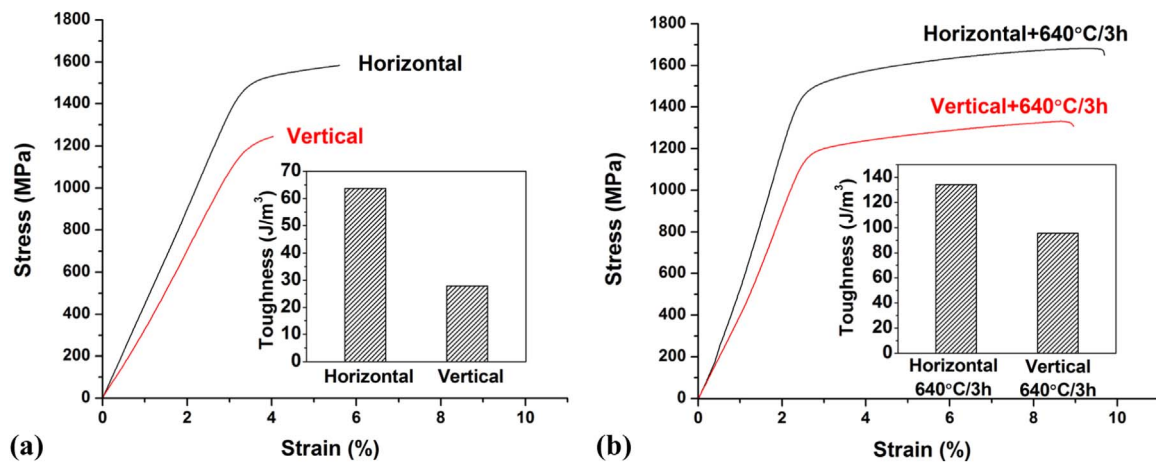
Fig. 10. Examined tensile stress-strain curves and calculated toughness of (a) as-fabricated and (b) heat-treated specimens (η=215.28 J/mm^3).

intrinsic residual stress is believed to be an important factor enhancing the strength and ductility of SLM-processed parts. Thirdly, it is well acknowledged that the thermal stress and phase transformation stress would become the driving force of recrystallization during the heat treatment process. As described by Jandaghi et al. [31], the residual strain and stress formed within workpiece would drive the recrystallization of deformed grains and give rise to the variation of grain size. By optimizing the time of heat treatment, refined equiaxed grains can be obtained [32]. This would improve the mechanical properties significantly. Besides residual strain and stress, there are many factors influencing the grain size after recrystallization such as treatment temperature, treatment time and original grain size. In future studies, the influence of above-mentioned factors on the mechanical properties of heat-treated SLM-processed parts shall be investigated.

5. Conclusion

(1) The 5CrNi4Mo tool steel parts fabricated by SLM were characterized by a heterogeneous microstructure, due to the distinctive and sophisticated thermal history within the melt pool. The cooling rate and maximum liquid flow velocity-magnitude near melt pool boundary were different at various regions of melt pool. At the bottom zone of melt pool, the high ΔT could lead to a high thermodynamics nucleation rate and the relatively large K_l guaranteed the high activity of solute atoms, hence significantly facilitating the refinement of microstructures. In contrast, the lower ΔT and K_l in the center/top zone implied weaker driving force of crystallization and diffusion ability of solute atoms, which accordingly resulted in a coarsed microstructure.

(2) The chemical composition distribution of SLM-processed parts was observed to be homogeneous, which was believed to be caused by insufficient time for diffusion of the alloying elements during the rapid solidification process. The carbides were not forming at the martensite boundary, which meant that the carbide formers tended to remain in solid solutions with iron rather than forming carbides.

(3) The ductility of as-fabricated specimens was dissatisfactory due to the heterogeneous microstructures and residual stress concentration. The different deformation mode during loading led to the different tensile properties between the vertically and horizontally built samples. The post-vacuum heat treatment had a significant influence on the tensile properties of the 5CrNi4Mo specimens. For the horizontally built specimens, the tensile strength increased marginally from 1576–1682 MPa; the elongation was elevated from 5.6–9.7%; the toughness was enhanced from 63.68 J/m^3 to 134.12 J/m^3. These promotions were mainly caused by pronounced relief of intrinsic residual stress and recrystallization effect. The equiaxed dimples with an average size about 1 μm were observed across the whole fracture surface, showing a highly ductile fracture.
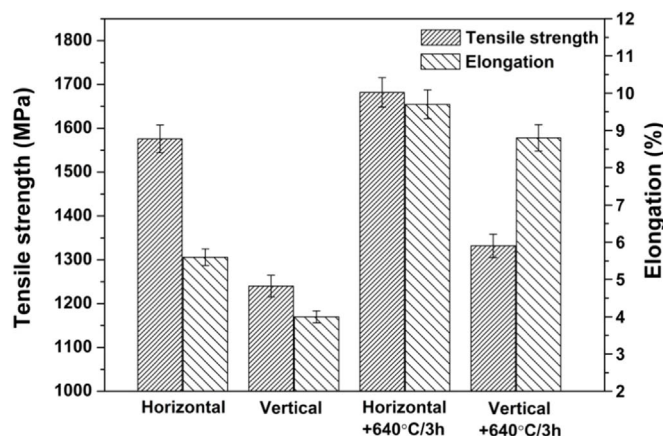
Fig. 11. Tensile properties (tensile strength and elongation) of SLM-processed parts of as-fabricated and heat-treated (η=215.28 J/mm^3).
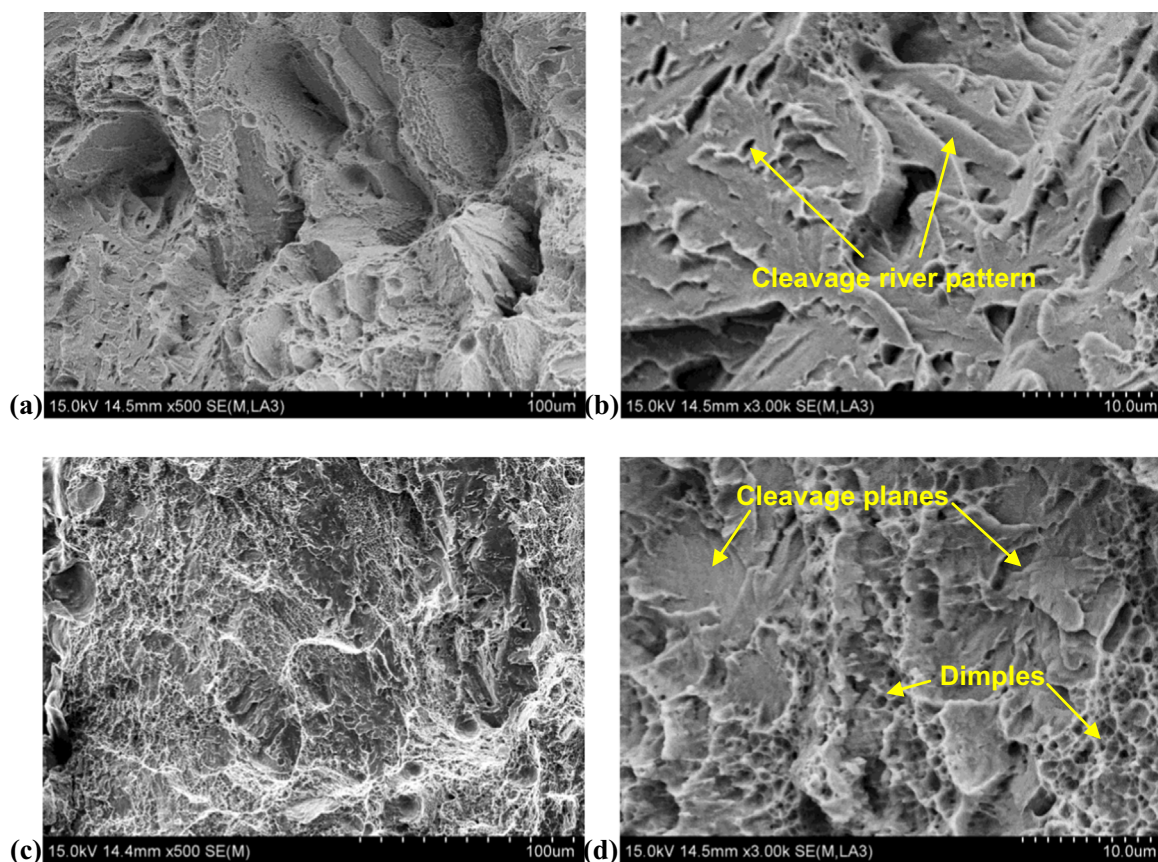
Fig. 12. Typical FE-SEM images taken from the tensile fracture surfaces of SLM-processed specimens fabricated along vertical orientation (a, b) and horizontal orientation (c, d). (For interpretation of the references to color in this figure, the reader is referred to the web version of this article.)
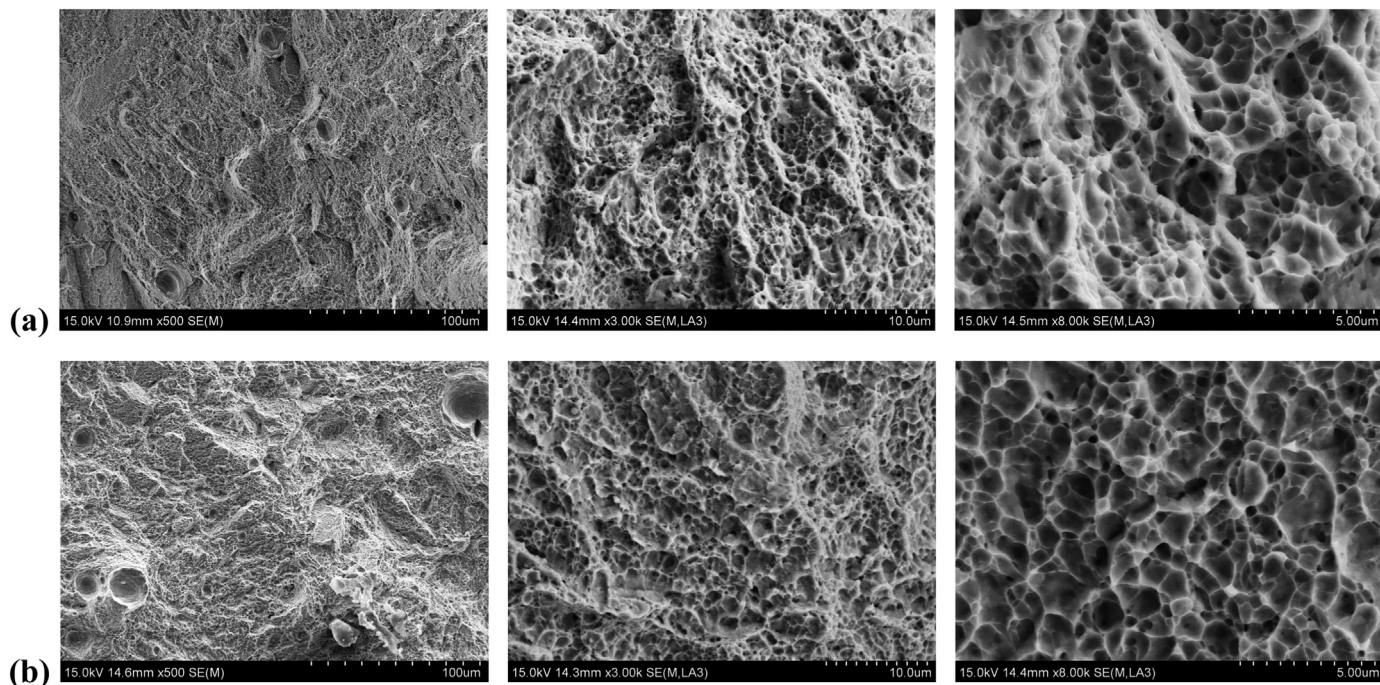

Fig. 13. Typical FE-SEM images taken from the tensile fracture surfaces of heat-treated specimens fabricated along vertical orientation (a) and horizontal orientation (b).

References

[1] M. Akita, Y. Uematsu, T. Kakiuchi, M. Nakajima, R. Kawaguchi, Defect-dominated fatigue behavior in type 630 stainless steel fabricated by selective laser melting, Mater. Sci. Eng. A 666 (2016) 19–26.

[2] J. Suryawanshi, K.G. Prashanth, S. Scudino, J. Eckert, O. Prakash, U. Ramamurty, Simultaneous enhancements of strength and toughness in an Al-12Si alloy synthesized using selective laser melting, Acta Mater. 115 (2016) 285–294.

[3] H. Alsalla, L. Hao, C. Smith, Fracture toughness and tensile strength of 316 L stainless steel cellular lattice structures manufactured using the selective laser melting technique, Mater. Sci. Eng. A 669 (2016) 1–6.

[4] D.Tomus, Y.Tian, P.A.Rometsch, M.Heilmaier, X.H.Wu, Influence of post heat treatments on anisotropy of mechanical behaviour and microstructure of Hastelloy-X parts produced by selective laser melting, Mater. Sci. Eng. A, 667, 2016. pp. 42–53.

[5] J. Sander, J. Hufenbach, L. Giebeler, H. Wendrock, U. Kühn, J. Eckert, Microstructure and properties of FeCrMoVC tool steel produced by selective laser melting, Mater. Des. 89 (2016) 335–341.

[6] R. Colaco, R. Vilar, Stabilisation of retained austenite in laser surface melted tool steels, Mater. Sci. Eng. A 385 (2004) 123–127.

[7] B.AlMangour, D.Grzesiak, J.-M.Yang, Nanocrystalline TiC-reinforced H13 steel matrix nanocomposites fabricated by selective laser melting, Mater. Des., 96, 2016. 150–161.

[8] M. Badrossamay, T.H.C. Childs, Further studies in selective laser melting of stainless and tool steel powders, Int. J. Mach. Tools Manuf. 47 (2007) 779–784.

[9] M.J. Holzweissig, A. Taube, F. Brenne, M. Schaper, T. Niendorf, Microstructural characterization and mechanical performance of hot work tool steel processed by selective laser melting, Metall. Mater. Trans. B-Proc. Metall. Mater. Proc. Sci. 46 (2015) 545–549.

[10] M.J. Faizabadi, G. Khalaj, H. Pouraliakbar, M.R. Jandaghi, Predictions of toughness and hardness by using chemical composition and tensile properties in microalloyed line pipe steels, Neural Comput. Appl. 25 (2014) 1993–1999.

[11] D.D. Gu, H.Q. Wang, D.H. Dai, F. Chang, W. Meiners, Y.-C. Hagedorn, K. Wissenbach, I. Kelbassa, R. Poprawe, Densification behavior, microstructure evolution, and wear property of TiC nanoparticle reinforced AlSi 10 Mg bulk-form nanocomposites prepared by selective laser melting, J. Laser Appl. 27 (2015) S17003.

[12] M.S. Khorrami, M.A. Mostafaei, H. Pouraliakbar, A.H. Kokabi, Study on microstructure and mechanical characteristics of low-carbon steel and ferritic stainless steel joints, Mater. Sci. Eng. A 608 (2014) 35–45.

[13] J.G. Sanjayan, A. Nazari, H. Pouraliakbar, FEA modelling of fracture toughness of steel fibre-reinforced geopolymer composites, Mater. Des. 76 (2015) 215–222.

[14] D.H. Dai, D.D. Gu, Thermal behavior and densification mechanism during selective laser melting of copper matrix composites: simulation and experiments, Mater. Des. 55 (2014) 482–491.

[15] P.P. Yuan, D.D. Gu, Molten pool behaviour and its physical mechanism during selective laser melting of TiC/AlSi10Mg nanocomposites: simulation and experiments, J. Phys. D.-Appl. Phys. 48 (2015) 035303.

[16] B.J. Keene, Review of data for the surface tension of pure metals, Int. Mater. Rev. 38 (1993) 157–192.

[17] D. Wang, C.H. Song, Y.Q. Yang, Y.C. Bai, Investigation of crystal growth mechanism during selective laser melting and mechanical property characterization of 316 L stainless steel parts, Mater. Des. 100 (2016) 291–299.

[18] A. Hussein, L. Hao, C. Yan, R. Everson, Finite element simulation of the temperature and stress fields in single layers built without-support in selective laser melting, Mater. Des. 52 (2013) 638–647.

[19] X.B. Su, Y.Q. Yang, Research on track overlapping during Selective Laser Melting of powders, J. Mater. Process. Technol. 212 (2012) 2074–2079.

[20] M. Das, V.K. Balla, D. Basu, S. Bose, A. Bandyopadhyay, Laser processing of SiC-particle-reinforced coating on titanium, Scr. Mater. 63 (2010) 438–441.

[21] D.D. Gu, Y.-C. Hagedorn, W. Meiners, G.B. Meng, R.J.S. Batista, K. Wissenbach, R. Poprawe, Densification behavior, microstructure evolution, and wear performance of selective laser melting processed commercially pure titanium, Acta Mater. 60 (2012) 3849–3860.

[22] H. Attar, K.G. Prashanth, A.K. Chaubey, M. Calin, L.C. Zhang, S. Scudino, J. Eckert, Comparison of wear properties of commercially pure titanium prepared by selective laser melting and casting processes, Mater. Lett. 142 (2015) 38–41.

[23] B. Song, S.J. Dong, H.L. Liao, C. Coddet, Manufacture of Fe-Al cube part with a sandwich structure by selective laser melting directly from mechanically mixed Fe and Al powders, Int. J. Adv. Manuf. Technol. 69 (2013) 1323–1330.

[24] Z.H. Liu, D.Q. Zhang, C.K. Chua, K.F. Leong, Crystal structure analysis of M2 high speed steel parts produced by selective laser melting, Mater. Charact. 84 (2013) 72–80.

[25] I. Hemmati, V. Ocelik, J.Th.M. De Hosson, Microstructural characterization of AISI 431 martensitic stainless steel laser-deposited coatings, J. Mater. Sci. 46 (2011) 3405–3414.

[26] H. Pouraliakbar, M. Hamedi, A.H. Kokabi, A. Nazari, Designing of CK45 Carbon Steel and AISI 304 Stainless Steel Dissimilar Welds, Mater. Res. -Ibero-Am. J. Mater. 17 (2014) 106–114.

[27] K. Kempen, L. Thijs, J. Van Humbeeck, J.P. Kruth, Processing AlSi 10 Mg by selective laser melting: parameter optimisation and material characterisation, Mater. Sci. Technol. 31 (2015) 917–923.

[28] X.M. Zhao, X. Lin, J. Chen, L. Xue, W.D. Huang, The effect of hot isostatic pressing on crack healing, microstructure, mechanical properties of Rene88DT superalloy prepared by laser solid forming, Mater. Sci. Eng. A 504 (2009) 129–134.

[29] Y. Zhong, L.F. Liu, S. Wikman, D.Q. Cui, Z.J. Shen, Intragranular cellular segregation network structure strengthening 316 L stainless steel prepared by selective laser melting, J. Nucl. Mater. 470 (2016) 170–178.

[30] C.L. Qiu, N.J.E. Adkins, M.M. Attallah, Selective laser melting of Invar 36: microstructure and properties, Acta Mater. 103 (2016) 382–395.

[31] M.R. Jandaghi, H. Pouraliakbar, M.K.G. Shiran, G. Khalaj, M. Shirazi, On the effect of non-isothermal annealing and multi-directional forging on the microstructural evolutions and correlated mechanical and electrical characteristics of hot-deformed Al-Mg alloy, Mater. Sci. Eng. A 657 (2016) 431–440.

[32] H. Pouraliakbar, S. Firooz, M.R. Jandaghi, G. Khalaj, A. Amirafshar, Combined effect of heat treatment and rolling on pre-strained and SPDed aluminum sheet, Mater. Sci. Eng. A 612 (2014) 371–379.